Silica material variation for Mn_xO_y-Na_2WO_4/SiO_2

M. Yildiz[a,1,*], Y. Aksu[b,2], U. Simon[c], T. Otremba[a,3], K. Kailasam[d,4], C. Göbel[d], F. Girgsdies[e], O. Görke[c], F. Rosowski[f], A. Thomas[d], R. Schomäcker[a], S. Arndt[a,5,*]

[a]*Technische Universität Berlin, Institut für Chemie, Technische Chemie, Sekr. TC8, Straße des 17. Juni 124, 10623 Berlin, Germany. yildizm@gtu.edu.tr[1], schomaecker@tu-berlin.de, torsten.otremba@integratedlabsolutions.com[3], arndt@bluebottle.com[5].*

[b]*Technische Universität Berlin, Institut für Chemie, Metallorganische Chemie & Anorganische Materialien, Straße des 17. Juni 115, 10623 Berlin, Germany. yilmazaksu@akdeniz.edu.tr[2].*

[c]*Technische Universität Berlin, Institut für Werkstoffwissenschaften und –technologien, Fachgebiet Keramische Werkstoffe, Sekr. BA3, Hardenbergstraße 40, 10623 Berlin, Germany. ulla.simon@ceramics.tu-berlin.de, oliver.goerke@ceramics.tu-berlin.de.*

[d]*Technische Universität Berlin, Institut für Chemie, Funktionsmaterialen, Sekr. BA2, Hardenbergstraße 40, 10623 Berlin, Germany. arne.thomas@tu-berlin.de, kamal@inst.ac.in[4], caren.goebel@tu-berlin.de.*

[e]*Fritz-Haber-Institut der Max-Planck-Gesellschaft, Abteilung Anorganische Chemie, Faradayweg 4-6, 14195 Berlin, Germany. girgsdie@fhi-berlin.mpg.de.*

[f]*BasCat UniCat BASF JointLab, Technische Universität Berlin, Sekretariat EW K 01, Hardenbergstraße 36, 10623 Berlin, Germany. frank.rosowski@basf.com.*

**Corresponding authors: yildizm@gtu.edu.tr; arndt@bluebottle.com.*

[1]*Present Address: Gebze Technical University, Department of Chemistry, 41400 Gebze, Kocaeli, Turkey. yildizm@gtu.edu.tr.*

[2]*Present Address: Akdeniz University, Faculty of Engineering, Department of Material Science and Engineering, Dumlupinar Bulvari, 07058 Antalya, Turkey. yilmazaksu@akdeniz.edu.tr.*

[3]*Present Address: ILS Integrated Lab Solutions GmbH, Max-Planck-Strasse 3, 12489 Berlin, Germany. torsten.otremba@integratedlabsolutions.com.*

[4]*Present Address: Institute of Nano Science and Technology, Habitat Centre, Phase-10, Sector-64, 160062 Mohali, Punjab, India. kamal@inst.ac.in.*

[5]*Present Address: PCK Raffinerie GmbH, Passower Chaussee 111, 16303 Schwedt/Oder, Germany. arndt@bluebottle.com.*

Abstract

The oxidative coupling of methane (OCM) is one of the best methods for the direct conversion of methane. Among the known OCM catalysts, Mn_xO_y-Na_2WO_4/SiO_2 is a promising candidate for an industrial application, showing a high methane conversion and C_2 selectivity, with a good stability during long-term catalytic activity tests. In the present study, some results have been already published and discussed briefly in our previous short communication [Yildiz 2014]. However, we herein investigated comprehensively the influence of various silica support materials on the performance of the Mn_xO_y-Na_2WO_4/SiO_2 system in the OCM by means of *ex situ* and *in situ* XRD, BET, SEM and TEM characterization methods and showed new results to reveal possible support effects on the catalyst. The catalytic performance of most Mn_xO_y-Na_2WO_4/SiO_2 catalysts supported by different silica support materials did not differ substantially. However, the performance of the SBA-15 supported catalyst was outstanding and the methane conversion was nearly twofold higher in comparison to the other silica supported catalysts at similar C_2 selectivity as shown before in the communication [Yildiz 2014]. The reason of this substantial increase in performance could be the ordered mesoporous structure of the SBA-15 support material, homogeneous dispersion of active components and high number of active sites responsible for the OCM.

Keywords: Oxidative Methane Coupling, OCM, Mn_xO_y-Na_2WO_4/SiO_2, Silica Support Material Variation, Mesoporous Silica, SBA-15, MCM-41.

1. Introduction

According to the statistical review on the worldwide energy resources, the proven reserves contain 187.1 trillion cubic meters natural gas by the end of 2014 [1]. Natural gas is used for home and industrial heating and the generation of electrical power, but it is still an underutilized resource for chemicals and liquid fuels. Since the reserves are far away from industrial areas and the high costs of building pipelines for transportation, on-site conversion of methane, the main constituent, to more useful chemicals (e.g. ethylene, methanol) could be of great importance for using it more effectively in industry [2-8].

Generally, there are two different ways for CH_4 utilization: the indirect and the direct way. All indirect methods for CH_4 conversion require a highly endothermic and expensive synthesis gas step. The disadvantages of indirect methods could be avoided by direct conversion of CH_4 into value added compounds. One of the most important direct reactions is the oxidative coupling of methane (OCM) to ethane and ethylene. The targeted reaction and the desired product are shown in equation (1):

$$aCH_4 + bO_2 \rightarrow cC_2H_6 + dC_2H_4 + eH_2O \qquad (1)$$

However, up to date, this reaction has not reached the stage of commercial application, even though a large number of catalysts [9-11] have been tested since the first attempts by Keller *et al.* and Hinsen *et al.* [12, 13]. Methane is the most stable hydrocarbon, having the strongest C-H bond; therefore, the activation of this bond is most difficult [14]. Thus, the oxidative coupling of methane occurs at high temperatures, usually above 700 °C. At these high temperatures, many catalysts suffer

from severe stability and selectivity problems, e.g. Li/MgO as shown by Arndt *et al.* [15, 16].

The most vital challenge for the OCM is the stability of the catalyst. Among the known OCM catalysts, Mn_xO_y-Na_2WO_4/SiO_2 is a promising one [17, 18] in the literature for the commercialization of an industrial process [19-28]. Moreover, its catalytic performance (CH_4 conversions of 20-30% at C_2 selectivities of approximately 70-80%) is superior to the most OCM catalysts.

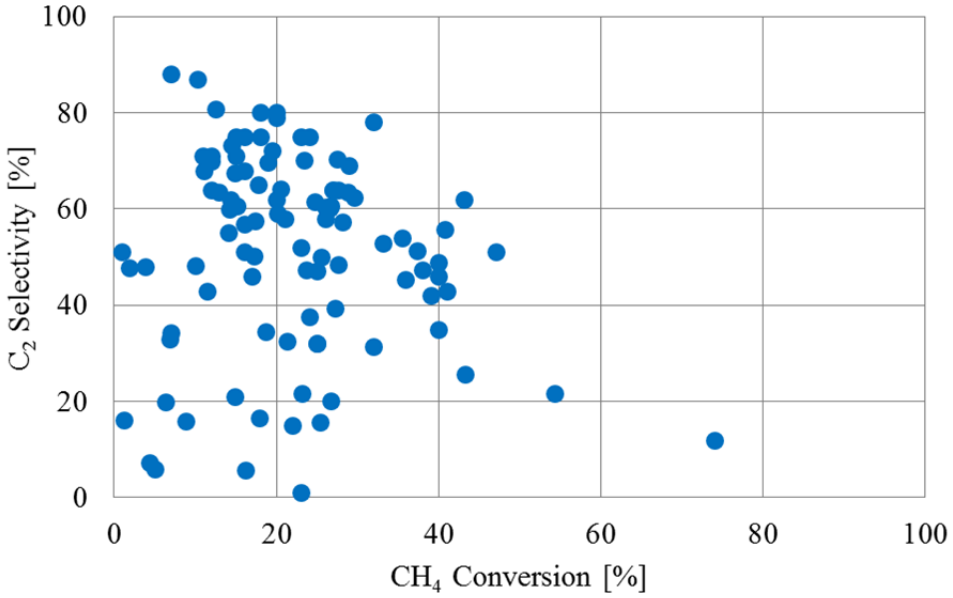

Figure 1. A general comparison of some OCM catalysts published in literature (approximately 100 results were selected randomly from [10]).

Besides that it is a very difficult issue to compare own results with reported results in literature due to the very different conditions and the very temperature-sensitive features of the OCM reaction. Therefore, as seen in Figure 1 some selected results from literature are broadly scattered, prohibiting any conclusion.

Although the incipient wetness impregnation has been the most applied method

for the catalyst preparation, different preparation procedures for the Mn_xO_y-Na_2WO_4/SiO_2 like solution combustion, flame spray pyrolysis and sol-gel routes have been used in recent years [29-32]. Besides that, Hiyoshi and Ikeda showed an improving effect of alkali chloride addition into Mn_xO_y-Na_2WO_4/SiO_2. However, the most important challenge was the deactivation due to the evaporation of alkali metal chlorides from the catalyst [33].

Liu *et al.* carried out experiments with SiC as a support material for this trimetallic system and the Mn_xO_y-Na_2WO_4/SiC showed similar performance compared to the silica supported catalyst [34]. Yu *et al.* applied La_2O_3, CeO_2, Pr_6O_{11}, Nd_2O_3, Sm_2O_3, Dy_2O_3, Yb_2O_3 and SiO_2 compounds as support material for only Na_2WO_4 as active component. However, some of the used support materials like Sm_2O_3 and Nb_2O_3 are known as active catalysts themselves for the OCM [35]. Wang *et al.* and Pak *et al.* investigated Mn_xO_y-Na_2WO_4/SiO_2 and Mn-Na_2WO_4/MgO systems to figure out the active sites and the elementary reactions. Na-O-Mn species as active site, sodium as suppressing component for the CH_4 total oxidation, tungstate ions as stability providing component and surface oxygens as hydrogen abstracting species from CH_4 were concluded [36, 37]. Recently, Elkins and Hagelin-Weaver have compared Mn_xO_y-Na_2WO_4/SiO_2, Mn-Na_2WO_4/MgO, Mn_xO_y/SiO_2 and Na_2WO_4/SiO_2 and indicated that except Mn_xO_y-Na_2WO_4/SiO_2, other compared catalyst showed lower methane conversion in the OCM. Furthermore, Na_2WO_4 and Mn_2O_3 phases were more stable in the Mn_xO_y-Na_2WO_4/SiO_2 in comparison to that of Mn-Na_2WO_4/MgO and the reason of that was suggested the α-cristobalite phase of the SiO_2 support material [38]. Serres *et al.* increased the loading amount of active compounds with respect to the support material to improve the performance of the catalyst sustaining its high C_2 selectivity.

After they had concluded to hinder a substantial decreasing of the surface area of the catalyst at high loadings, the SiO_2 support material of the Mn_xO_y-Na_2WO_4/SiO_2 catalyst was replaced with porous SiC and α-Al_2O_3 expecting a catalyst with high surface area at high loading of the active components. Increasing the amount of the active compounds improved evidently the performance of the catalyst but it is limited to a proper loading level. While a replacement of the SiO_2 support with porous SiC providing a high surface area upgraded the activity, an application of α-Al_2O_3 instead of SiO_2 resulted in poor performance due to a differently composed surface in the absence of silica. In spite of the improvements of catalyst activity in that study, even the performance of the optimized Mn-Na-W-/SiC do not reach to a La based catalyst, La/Sr/CaO [39].

In a previous study [40], we investigated a wide-range variety of support materials for the Mn_xO_y-Na_2WO_4/SiO_2 catalyst, in order to test alternative support materials to SiO_2, which could suppress the pathway of the total oxidation of methane and found that SiO_2, TiO_2-rutile and SiC were the most suitable support materials. Furthermore, a Mn_xO_y-Na_2WO_4 catalyst without support material showed remarkable activity, raising questions on the role of the support material. Recently, we showed the catalytic activity results of the differently performing Mn_xO_y-Na_2WO_4/SiO_2 catalysts (Cat-H, Cat-M and Cat-L) prepared from three various silica materials, superiority of the SBA-15 supported Mn_xO_y-Na_2WO_4 and discussed concisely some results on BET surface area, XRD phase analysis and SEM-EDX images [41]. Herein, we studied more intensively the effect of different SiO_2 materials as support for the Mn_xO_y-Na_2WO_4/SiO_2 catalyst and the structural impact on the catalytic performance. Hence, we included also the previously published results of our short communication in this paper for the sake of completeness of the scientific discussion.

2. Experimental Part

2.1. Support Material Preparation

Each silica type material has been given a code, since there were many different types of silica support materials. All of the used silica support materials, their origins, specific surface areas and the codes are shown in Table 1. The preparation method of ordered mesoporous silica material produced in the laboratory of the Functional Materials Department of the Technische Universität Berlin is explained in the supporting information.

2.2. Catalyst Preparation

Eleven different silica supported Mn_xO_y-Na_2WO_4 catalysts were prepared by a standard two-step wet impregnation procedure and a mixed milling method as explained in the supporting information. The amounts of the active components were 5 wt% Na_2WO_4 and 2 wt% Mn_xO_y. Manganese was present in the form of manganese oxides or Mn-containing mixed oxides, however, the loading was calculated for pure Mn. For a structural analysis after the reaction, it is necessary to retrieve the catalysts. With the applied quartz sand this is not possible, because its particle size distribution is too large and overlaps with the particle size of the catalysts. Therefore, Arndt *et al.* [16] performed a separation method using quartz balls in their previous work and also in this study the same method was adopted.

Table 1. The origin, code, specific surface area, pore volume, pore diameter of silica support materials (S1-S11) used in "3.1. Characterization" and "3.2. Catalysis" parts and ordered mesoporous silica materials (SBA-15, SBA-15-ACS) used in "3.3. Detailed Investigation of Selected Catalysts" part.

Code	Origin of Support	Surface Area [m^2/g]	Pore Volume[a] [cm^3/g]	Pore Diameter[b] [nm]
S1	BASF, D11-10	105	0.60	23.65
S2	Sigma-Aldrich, grade 923, pore size 30A°	492	0.39	3.23
S3	Sigma, fumed, particle size 0,007µ	368	0.91	12.23
S4	Evonik Industries, Aerosil TT 600	170	0.19	6.19
S5	Evonik Industries, VP Aeroperl R 806/30	206	1.68	28.81
S6	Evonik Industries, Aerosil OX 50	51	0.58	48.67
S7	Evonik Industries, Aerosil 380	348	0.94	13.84
S8	Evonik Industries, Aerosil 300	475	1.56	16.49
S9	Evonik Degussa GmbH, Sipernat D10	130	1.10	29.68
S10	Evonik Degussa GmbH, Sipernat 310	552	1.46	9.36
S11	TU Berlin, SBA-15	437	0.58	5.20
SBA-15[c]	TU Berlin	617	0.69	4.97
SBA-15-ACS[d]	ACS Material, LLC	624	1.21	7.61

Adapted from [42]. [a]Single point adsorption total pore volume of pores. [b]BJH adsorption average pore diameter. [c]This material was also used in [41]. [d]This material was purchased from ACS Materials LLC to have SBA-15 as a different source and comparison.

2.3. Catalyst Characterization

The catalysts prepared and tested in the wide-range silica variation work (part 3.1 and part 3.2) were characterized via nitrogen physisorption and *ex situ* X-Ray diffraction. In the detailed investigation (part 3.3) prepared and tested catalysts were characterized by nitrogen physisorption, *ex situ* and *in situ* X-Ray diffraction, scanning electron microscopy/energy-dispersive X-ray spectroscopy and transmission electron microscopy. The specific surface area was determined by a Micromeritics Gemini III 2375 Surface Area Analyzer, using N_2 adsorption at -196 °C. Before measuring, the samples were degassed at 300 °C and 0.15 mbar at least for 30 minutes. The surface areas were calculated by the method of Brunauer, Emmett and Teller (BET). Powder X-Ray diffractograms (XRD) were obtained ($CuK\alpha_1$ radiation wavelength 0.154 nm) using Bruker AXS D8 ADVANCE X-ray diffractometer. The angle variation was performed from 2° to 90°, with a step size of 0.008°. The diffractograms were analyzed with the program Diffrac.suite EVA. *Ex situ* XRD measurements of selected catalysts (RCat-H, RCat-M and RCat-L) were performed on a Bruker AXS D8 ADVANCE DAVINCI diffractometer in Bragg-Brentano mode with a LYNXEYE position sensitive detector (Ni filtered CuKα radiation). Phase compositions of various *ex situ* and *in situ* XRD results were calculated from whole powder pattern fitting using the Rietveld method with DIFFRAC^{plus} TOPAS. The phase amounts are given as weight fractions and refer to the sum of all observed crystalline phases. The *in situ* XRD data were collected in Bragg-Brentano geometry on a STOE theta/theta diffractometer equipped with a

DECTRIS MYTHEN1K position sensitive detector (Ni filtered CuKα radiation) and an Anton Paar XRK 900 *in situ* reactor chamber. The gas feed was mixed by means of Bronkhorst mass flow controllers, using He as inert balance gas at a total flow rate of 100 ml/min. The effluent gas composition was monitored with a Pfeiffer OmniStar quadrupole mass spectrometer. Since the sample holder of the *in situ* chamber has to be filled with catalyst, the amount of the catalyst for the analysis depended strongly on its volume (high or low dense material) and for this reason the amount of analyzed catalyst was not defined. For *in situ* XRD analysis of the OCM catalyst, temperature was increased up to 750 °C in two hours and then the first *in situ* XRD measurement was recorded after 27 minutes. Afterwards, in every 27 minutes one measurement was achieved and totally 21 measurements were recorded. The duration of the *in situ* XRD characterization of the OCM catalyst was 9 hours. The flow rate was 100 ml/min with the feed gas composition of CH_4:O_2:He = 4:1:4. For *in situ* XRD analysis of the calcination process, the measurements were carried out without reactant flow under He:O_2 atmosphere with the flow rate 79:21 ml/min and temperature program is given in supplementary information. The surface microstructure (morphology and particle size) and chemical composition of the samples were studied by scanning electron microscopy (SEM) at the Department of Electron Microscopy, ZELMI, TU Berlin. A small amount of the sample powder was placed on a conducting carbon pad (Plano GmbH, Germany) and sputtered with a thin carbon layer. The investigations were performed by means of a JXA-8530F microprobe (JEOL GmbH, Germany) equipped with a field emission source. Qualitative chemical analysis and beam scan mapping were carried out by 20kV acceleration voltage with integrated energy dispersive X-ray spectroscopy using an SDD detector. Transmission electron microscopy (TEM) images were obtained on a FEI

Tecnai 20 microscope, using carbon-coated copper grids (the specimens were loaded directly onto the copper grids; no solvent dispersion was used).

2.4. Catalytic Tests

The details about the parallel testing reactor set-up and single reactor set-up used to perform catalytic activity tests in the present study and the contribution of the gas phase reactions can be found in supplementary materials (Table S1). However, since reaction conditions are important for any comparison, herein they are also mentioned briefly. 50 mg catalyst diluted with approximately 1.5 ml quartz sand, 750 °C temperature, 60 ml/min gas flow and a feed gas composition of CH_4:O_2:N_2 = 4:1:4 (methane and synthetic air as oxygen source) and particle size below 200 μm were used for the catalytic activity tests in the parallel testing reactor. The only differences for the single reactor tests were the used catalyst amount (100 mg) and the applied temperatures (725 °C for the first 5 h, 750 °C for the second 5 h and 775 °C for the last 5 h).

3. Results & Discussion

3.1. Characterization

3.1.1. Specific Surface Area

The BET surface areas of silica supported fresh and spent catalysts are shown in Table 2. The detailed information about the pure silica materials are presented in Table 1 (The BET isotherm graphics of all used silica support materials are shown in Figure S1-S13 in supplementary information). After the calcination process, the BET surface areas of the supports decreased substantially, even if they had a high surface area at the beginning. The reason of this reduction is the phase transformation of the amorphous

272 silica into highly cristalline α-cristobalite phase during the calcination process [17, 28,
273 43-46]. The surface areas of the catalysts were between 5-8 m^2/g, except S2 type silica
274 supported catalyst. The lowest surface area belonged to S2-type silica supported catalyst
275 with 2 m^2/g and its surface area increased to 3 m^2/g after reaction, while the surface area
276 of other catalysts decreased to 4-6 m^2/g range.
277
278 Table 2. The specific surface areas of 2 wt% Mn_xO_y-5 wt% Na_2WO_4/SiO_2 catalysts in
279 m^2/g. S: Silica support material (see Table 1).

Catalyst	Surface area (m^2/g)		Catalyst	Surface area (m^2/g)	
	Fresh	Spent		Fresh	Spent
Mn_xO_y-Na_2WO_4/S1	8	4	Mn_xO_y-Na_2WO_4/S7	6	5
Mn_xO_y-Na_2WO_4/S2	2	3	Mn_xO_y-Na_2WO_4/S8	6	4
Mn_xO_y-Na_2WO_4/S3	7	5	Mn_xO_y-Na_2WO_4/S9	5	4
Mn_xO_y-Na_2WO_4/S4	7	5	Mn_xO_y-Na_2WO_4/S10	8	6
Mn_xO_y-Na_2WO_4/S5	6	5	Mn_xO_y-Na_2WO_4/S11	5	5
Mn_xO_y-Na_2WO_4/S6	7	5			

280

281 **3.1.2. X-ray Diffraction**

282 Figure 2 and Table S2 show the detected phases of the different type of silica material
283 supported catalysts. SiO_2 (α-cristobalite) was the main phase for all catalysts. SiO_2
284 (tridymite) and Na_2WO_4 phases were detected in all catalysts, except S10 supported
285 sample (Figure 2). Besides that, Na_4WO_5 was also found in the catalysts except S1, S9
286 and S10 supported samples. The patterns identified as Mn_2O_3 might be also explained as
287 braunite ($MnMn_6SiO_{12}$) phase, since patterns of Mn_2O_3 and $MnMn_6SiO_{12}$ are very

similar and overlap.

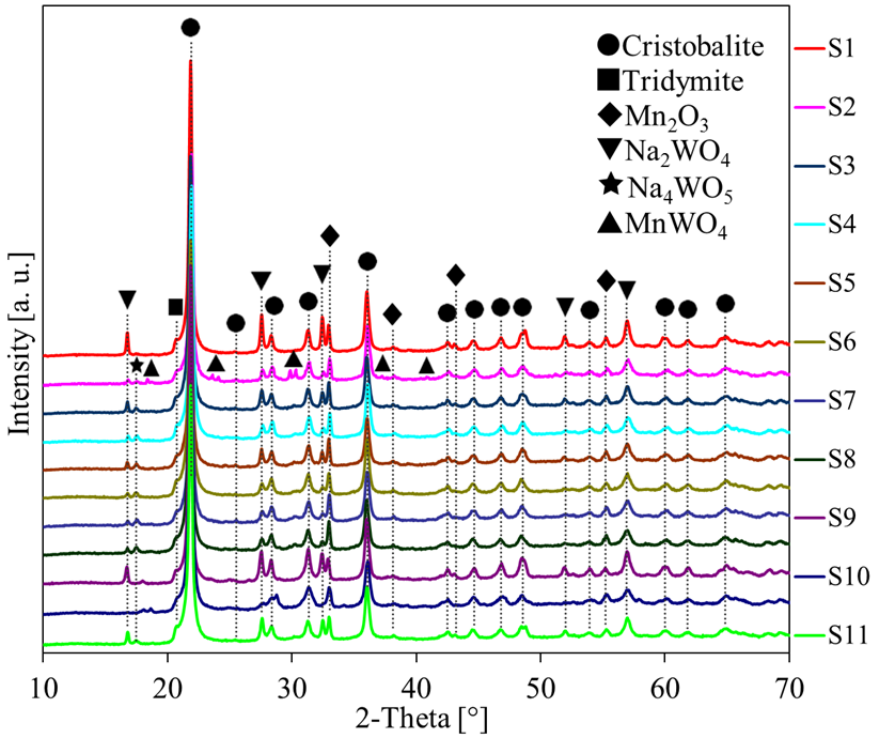

Figure 2. XRD patterns of all silica supported Mn_xO_y-Na_2WO_4 catalysts. Figure reprinted from [42] with permission from DGMK.

3.2. Catalysis

The catalytic experiments were carried out in the parallel test reactor set-up using packed-bed, linear, tubular reactors made of quartz glass as described in supplementary materials. The catalytic activity of all silica supported catalysts can be found in supplementary materials. Stability is of high importance for potential practical application of a catalyst. For this reason, the CH_4 conversion is shown as a function of time on stream in Figure 3. All tested silica supported catalysts were stable within the observed time, only slight deactivation was seen.

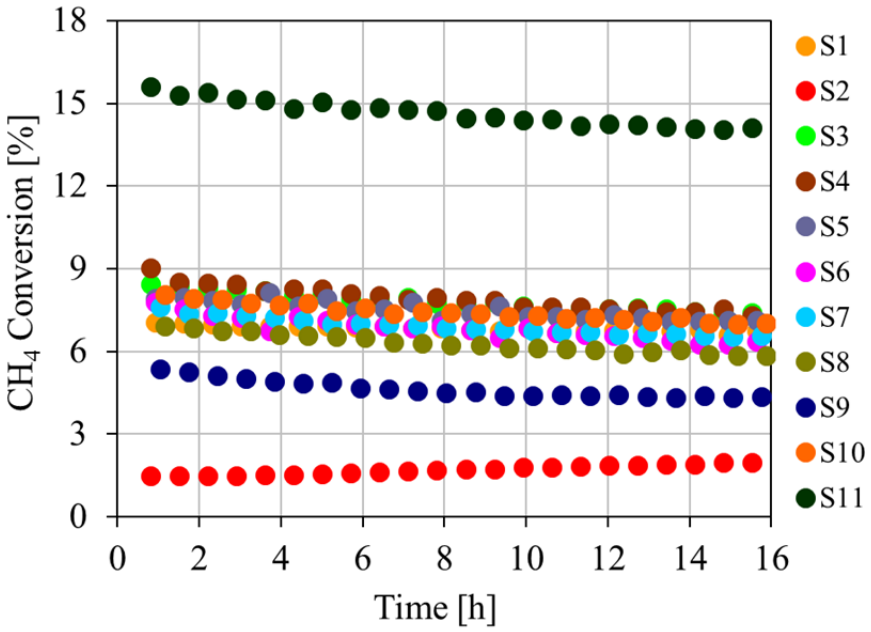

Figure 3. Methane conversion vs. time on stream. Reaction conditions: 750 °C, 50 mg catalyst diluted in 1.5 ml quartz sand, particle size of catalyst ≤ 200 µm, flow rate of 60 ml/min and feed gas composition of CH_4:O_2:N_2 = 4:1:4. Figure reprinted from [42], with permission from DGMK.

The CH_4 conversions of all prepared silica supported Mn_xO_y-Na_2WO_4 catalysts were very similar 5-7% (Table 3), except for S2 and S11 supported catalysts. The catalytic performances did not differ substantially. They all showed very similar CH_4 conversion, C_2 selectivity and C_2 yield (Table 3 and Figure S14), except S2 and S11 silica supported samples. Besides that, activity results of blank samples showed that all silica support materials were inert for the OCM (in supplementary materials). All catalysts were very selective towards the desired C_2 products and the selectivity values were between 60-80 %. The performance of the S11 (SBA-15) supported catalyst was outstanding at our test conditions with approximately 14% methane conversion and 70% C_2 selectivity. This means that the catalyst showed two fold CH_4 conversion at

very similar C_2 selectivity levels in comparison to other samples. On the other hand, the C_2H_6/C_2H_4 ratio was 1.1 for SBA-15 supported Mn_xO_y-Na_2WO_4, while this ratio was approximately 2 for the other silica supported catalysts (Table 3).

Table 3. Catalytic activity results of all tested silica supported catalysts after approx. 16 h time on stream. (For reaction conditions, see Figure 3).

Catalyst	**Performance**	**X-CH_4 [%]**	**S-C_2 [%]**	**Y-C_2 [%]**	**C_2H_6/C_2H_4**
Mn_xO_y-Na_2WO_4/S1	Medium	6.7	52.9	3.6	2.4
Mn_xO_y-Na_2WO_4/S2	Low	2.0	63.6	1.3	5.7
Mn_xO_y-Na_2WO_4/S3	Medium	7.4	61.3	4.5	2.0
Mn_xO_y-Na_2WO_4/S4	Medium	7.3	60.7	4.5	2.2
Mn_xO_y-Na_2WO_4/S5	Medium	7.1	68.9	4.9	1.9
Mn_xO_y-Na_2WO_4/S6	Medium	6.4	55.4	3.5	2.5
Mn_xO_y-Na_2WO_4/S7	Medium	6.6	62.6	4.2	2.3
Mn_xO_y-Na_2WO_4/S8	Medium	5.9	57.4	3.3	2.6
Mn_xO_y-Na_2WO_4/S9	Medium	4.4	80.3	3.5	2.5
Mn_xO_y-Na_2WO_4/S10	Medium	7.0	75.8	5.4	1.8
Mn_xO_y-Na_2WO_4/S11	High	14.1	73.4	10.4	1.1

The difference in C_2H_6/C_2H_4 ratio is the evidence that the Mn_xO_y-Na_2WO_4/SBA-15 is superior to the other catalysts with regard to the production of C_2H_4 which is the most desired product in the OCM. On the other hand, S2 type silica supported catalyst did not show the familiar high performance of conventional Mn_xO_y-Na_2WO_4/SiO_2 system, although there is no evident reason for this deviation.

Although only SiO_2 (cristobalite, tridymite) and Mn_2O_3 or $MnMn_6SiO_{12}$ (braunite) phases were detected in the S10 type (Evonik Degussa GmbH, amorphous SiO_2) supported catalyst, its performance was similar to other tested Mn_xO_y-Na_2WO_4/SiO_2 catalysts. When the XRD patterns of all catalysts are examined in detail (Figure 2), it can be seen that except for the S2 supported catalyst, all patterns seem similar to pattern of S1 supported catalyst and also SBA-15 (S11) supported catalyst has the same phases (Figure S15). The detected $MnWO_4$ phase was only found on the S2 supported catalyst, as shown in Figure S15.

Although there are some discussions on $MnWO_4$ phase in literature [28, 36], its role in the OCM is still unclear. It is really interesting that the S2 supported sample is the only catalyst which contains the $MnWO_4$ phase among the other silica supported catalysts. Moreover, it is almost inactive in the OCM and performed poorest. Therefore, it is questionable whether the presence of $MnWO_4$ phase in the fresh catalyst has lessened influence on the performance of the catalyst or not (shown also in Figure S16). On the other side, S11 supported catalyst showed an excellent performance, while the performance of S1 supported catalyst was representative for all the rest.

3.3. Detailed Investigation of Selected Catalysts

All silica supported samples can be sorted as high-, medium- and low-performance catalysts (Table 3). Herein, S2 supported catalyst as low performance catalyst, S1 supported catalyst as example for medium performance catalyst and S11 supported one as high performance catalyst were selected in order to characterize them structurally in detail both before and after the OCM reaction. For this investigation the three catalysts were reproduced as described in supporting information using S1, S2 and reproduced

SBA-15 support materials and were denominated with new codes as Cat-H, Cat-M and Cat-L (the letters stand for performance types; H: high, M: medium, L: low). Therefore, the reproduced samples were characterized and tested newly in this subsection to exclude batch related differences. All XRD analyses (Figure S16-S17), specific surface areas (Table S3 and Figure S18) and elemental analysis data (Table S4) of those catalysts are found in the supporting information.

3.3.1. Phase Analysis

In the *in situ* XRD experiments, reproduced Cat-H (RCat-H, prepared by applying SBA-15 support material purchased from ACS Materials), reproduced Cat-M (RCat-M, prepared by applying S10 type silica support material) and reproduced Cat-L (RCat-L, prepared by applying S2 type silica support material) were used due to full consumption of Cat named catalysts. All results about the RCat named catalysts shown in Table S5-S7 prove that the catalysts were reproduced successfully.

3.3.1.1. *In Situ* X-ray Diffraction Analysis during the OCM Reaction

We performed *in situ* XRD experiments for the catalysts in order to detect which phases are present in the catalyst under OCM reaction conditions. Figure 4 shows the phase analysis of *in situ* XRD patterns of RCat-H (Figures of RCat-M and RCat-L can be seen in Figure S19-S20 because of high similarity with the Figure of RCat-H). It can be clearly seen in the figures that under reaction conditions some structural changes take place for all three catalysts.

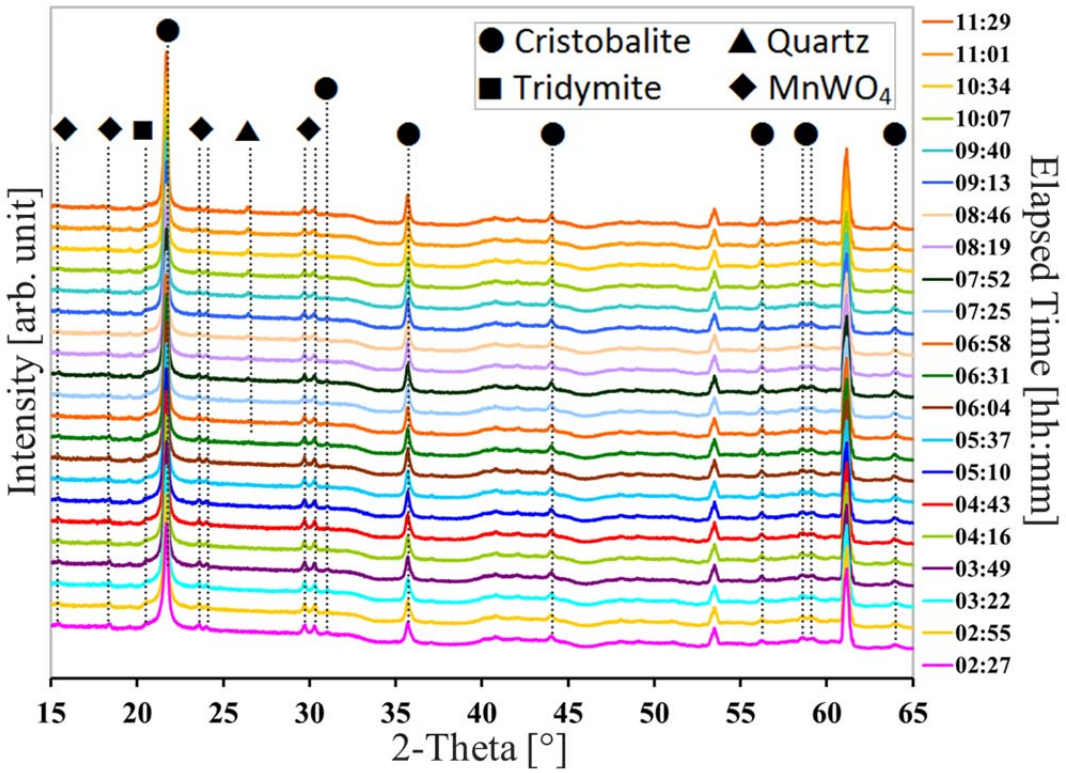

375

376 Figure 4. *In situ* XRD patterns of RCat-H catalyst.

377

378 Cristobalite, tridymite, braunite ($MnMn_6SiO_{12}$), $MnWO_4$ and Na_2WO_4 phases
379 were detected in the fresh catalyst of RCat-H when the *ex situ* XRD patterns were
380 examined (Figure S21). Under reaction conditions cristobalite, tridymite, quartz and
381 $MnWO_4$ phases were detected (Figure 4). No Na_2WO_4 and braunite ($MnMn_6SiO_{12}$)
382 phases were detected by *in situ* measurements. Amongst the components used in the
383 preparation process, Mn and W were detected as $MnWO_4$ during the reaction. The
384 amount of $MnWO_4$ phase was approximately 0.7 wt% in the fresh RCat-H catalyst
385 determined in *ex situ* analysis, while it was determined averagely 7.5 wt% in the *in situ*
386 analysis (Table S8-S10). This substantial increase might mean that Mn and WO_4
387 species, which come from braunite ($MnMn_6SiO_{12}$) and Na_2WO_4 compounds, could form
388 the $MnWO_4$ phase under reaction conditions. Since the melting point of Na_2WO_4 is 698

°C, at the reaction temperature (750 °C) it becomes a liquid phase. This melted phase could facilitate the $MnWO_4$ formation reaction. Furthermore the fraction of the $MnWO_4$ phase decreased step by step from the beginning until the end of the *in situ* analysis (from 8.6 wt % to 5.5 wt %). Besides that, it is remarkable that a quartz phase of the silica support material starts to form after the first half of the analysis (after 6 h 31 min) and its intensity increases steadily (Figure 4 and Table S8-S10). The direction of this transformation is most probably from cristobalite phase to quartz phase. On the other hand the tridymite phase changes during the *in situ* analysis. Its amount increased approximately by 3 wt% until the end of the analysis. However, the main phase during the reaction was cristobalite with in average 86 wt% and the most intense pattern.

Cristobalite, tridymite, braunite ($MnMn_6SiO_{12}$), $MnWO_4$, Na_2WO_4 and $CaWO_4$ phases were detected in the fresh catalyst of RCat-M in the *ex situ* XRD patterns (Figure S22). On the contrary, under OCM conditions, cristobalite, tridymite, quartz, $MnWO_4$ and $CaWO_4$ phases could be detected (Figure S19). As in the *in situ* analysis of RCat-H catalyst, Na_2WO_4 and braunite ($MnMn_6SiO_{12}$) phases were also not detected in the *in situ* analysis of the RCat-M. The determination of phase amount for the RCat-M catalyst in the *in situ* measurements was only done until the middle of the analysis. Because of the high complexity of the supported three component catalyst, the amounts of phases were determined until the 13rd measurement (for 7 h 25 min elapsed). Since its amount is too low, approximately 0.5 wt %, with decreasing trend over time and because of very high number of 21 patterns, $CaWO_4$ phase cannot be shown in Figure S19. However, its pattern and also its amount which is in the fresh state of the catalyst can be seen in the *ex situ* XRD phase analysis in Figure S22. Although we did not use any Ca precursor during preparation of the catalyst, it is questionable why a phase containing Ca was

413 detected in the catalyst. The formation of a $CaWO_4$ phase might most probably be a Ca
414 impurity from the commercially purchased SiO_2 support material (Table S11-S12).
415 Even though its amount in the fresh catalyst was 1.11 wt%, it was 0.67 wt% in the first
416 *in situ* measurement and decreased to 0.37 wt% until the half of the analysis. However
417 $MnWO_4$ was again the only detectable active component under OCM conditions with in
418 average 6.5 wt%, showing decreasing trend (from 7.41 wt% to 4.89 wt%), while its
419 amount was only 0.51 wt% in the fresh catalyst in the *ex situ* XRD analysis. The
420 increasing amount of the $MnWO_4$ phase might have formed as explained in the case of
421 RCat-H catalyst above. On the other side, after 7 h, since the beginning of the *in situ*
422 analysis, a quartz phase started to form. Besides that, tridymite phase amount increased
423 from 4.70 wt% to 7.06 wt% until the half of the analysis. This tridymite amount was
424 very similar to the tridymite amount of RCat-H catalyst which was determined at the
425 end of the analysis. Furthermore, cristobalite, with in average 87 wt% at a usually
426 constant level, was the most abundant phase under the OCM conditions in the *in situ*
427 XRD experiments of RCat-M catalyst.

428 In the *in situ* XRD analysis of RCat-L catalyst, cristobalite, quartz, tridymite and
429 $MnWO_4$ phases were detected (Figure S20), while cristobalite, tridymite, braunite
430 ($MnMn_6SiO_{12}$), $MnWO_4$ and Na_2WO_4 were detected by the *ex situ* XRD analysis in the
431 fresh catalyst (Figure S23). Detected phases of RCat-H and RCat-L catalysts were
432 exactly the same in both *in situ* and also *ex situ* analyses. Na_2WO_4 and braunite
433 ($MnMn_6SiO_{12}$) phases could not be detected via *in situ* XRD measurements for RCat-L.
434 $MnWO_4$ was the only active compound including starting precursor elements during the
435 analysis. $MnWO_4$ amount of the fresh catalyst was approximately 1.7 wt%. On the other
436 hand, the amount of $MnWO_4$ phase decreased from 7.78 wt% to 5.75 wt% during

437 analysis over time. The increasing $MnWO_4$ amount, from 1.7 wt% to 7.78 wt%, can be
438 explained similarly to the cases of RCat-H and RCat-M. Besides, it is very pronounced
439 that the phase transformation of the silica support material into quartz phase started very
440 early in RCat-L in comparison to RCat-H and RCat-M. The first quartz phase pattern
441 was seen already 4 h 45 min after the analysis had been started. Until the end of the
442 analysis its amount increased drastically up to 15.96 wt%, while it was only 0.33 wt% at
443 the beginning. On the contrary, tridymite amounts were very close to each other and
444 constant with in average 4.7 wt% during the reaction. However, it is really remarkable
445 that the decreasing amount of the main cristobalite phase is substantial for the RCat-L
446 catalyst (from 87.65 wt% to 73.47 wt%). These changes between increasing amount of
447 quartz phase and decreasing amount of cristobalite phase indicate that the cristobalite
448 phase of silica transforms mostly into a quartz phase under OCM conditions.
449 In the *in situ* XRD analysis there are two highly intensive peaks around 54° and
450 61°. Since these are not present in the *ex situ* XRD analysis, it shows that these artifacts
451 come from the chamber used for *in situ* measurements. All *in situ* XRD analysis
452 patterns of RCat-H, RCat-M and RCat-L for the OCM reaction are available in
453 supplementary information.
454 It can be concluded for the three catalysts: The main phase is always cristobalite
455 and Na is the structural modifier for the SiO_2. A detected phase of active component is
456 always $MnWO_4$. No Na_2WO_4 and $MnMn_6SiO_{12}$ (braunite) phases could be detected.
457 Because, Na_2WO_4 (melting point: 698 °C) is in liquid phase under reaction conditions,
458 $MnWO_4$ forms from braunite and Na_2WO_4. Quartz phase formation (structural change
459 of silica support material) was observed, which was highest for RCat-L in comparison
460 to RCat-H and RCat-M. No major difference was observed between the three different

phases of silica (cristobalite, tridymite and quartz) in the *in situ* XRD analysis of RCat-H, RCat-M and RCat-L under the OCM conditions.

3.3.1.2. *In situ* X-ray Diffraction Analysis during the Calcination Process

The main phase of the support material of active Mn_xO_y-Na_2WO_4/SiO_2 catalyst is always cristobalite in both, the fresh catalysts and the catalysts under the OCM reaction conditions. However, during preparation of the catalyst the phase of the silica support material is not highly cristalline cristobalite phase but usually only amourphous silica. Furthermore, during the calcination process described in the supporting information, the amorphous phase of silica support material transforms into cristobalite. Palermo *et al.* showed that this kind of transformation is required for a good OCM performance [44]. Although normal transition temperature is 1500 °C [47], the presence of Na alkali metal lowers the transition temperature down to approximately 750 °C [44]. However, we always detect only transformed cristobalite phase in the *ex situ* XRD pattern of the fresh catalyst after the calcination process and it is not known precisely at which temperature this transformation takes place. The main idea of the *in situ* XRD analysis of the calcination process was to observe the transformation of amorphous silica to cristobalite during the calcination and to investigate whether there are some differences between the differently performing catalysts (Figure S24-27 and Table S13).

Catalyst precursors (after impregnation and drying process but not calcined) of RCat-H, RCat-M and RCat-L were used in the *in situ* XRD analysis of the calcination process. We also wanted to evaluate phase formations and/or transformations of active components via this analysis. However, the typical and characteristic patterns of tridymite, Mn_2O_3 or $MnMn_6SiO_{12}$ (braunite), Na_2WO_4, etc. were unfortunately not

observed in the *in situ* XRD analysis of the calcination process.

In the *ex situ* XRD phase analysis of RCat catalyst series, these phases were observable, even if their intensities were low. However, if we do not detect these phases during *in situ* XRD calcination analysis, this indicates that the calcination atmosphere might have a strong effect on the formation of phases. Because, while the *ex situ* XRD measurements were performed under atmospheric air, the *in situ* XRD measurements were performed under $He:O_2$ atmosphere with the flow rate 79:21 ml/min (The application of $He:O_2$ atmosphere was a requisite to operate the devices of the *in situ* set-up).

The phase transformation to cristobalite phase starts between 675 °C and 690 °C for the RCat-H, between 690 °C and 700 °C for the RCat-M, between 710 °C and 720 °C for the RCat-L. $MnWO_4$ phase, which was detected in some measurements during analyses, might come from the interaction of the molten Na_2WO_4 and the decomposition of $Mn(CH_3COO)_2$.

Thus, phase transformation of silica support material occurred, but at different temperatures ($T_{RCat\text{-}L}>T_{RCat\text{-}M}>T_{RCat\text{-}H}$) and $MnWO_4$ formation was detected during calcination process. See supporting materials for the applied temperature program, comparative XRD phase analyses and XRD pattern of each experiment.

3.3.2. Electron Microscopy (SEM-EDX/TEM)

Electron microscopy was used in order to reveal the morphology (shape, size), structure (crystallographic phase) and chemical composition of the different silica materials. The results are illustrated in Figure 5-7 and Figure S28-S32.

SEM images of Cat-H show elongated fibrous particles of the ordered SBA-15 material (Figure 5). The infiltrated catalyst precursor features similar chain-like structure, the fresh catalyst retains its morphology after the calcination. In contrast, catalytic testing destroyed the original microstructure of the SBA-15 material completely.

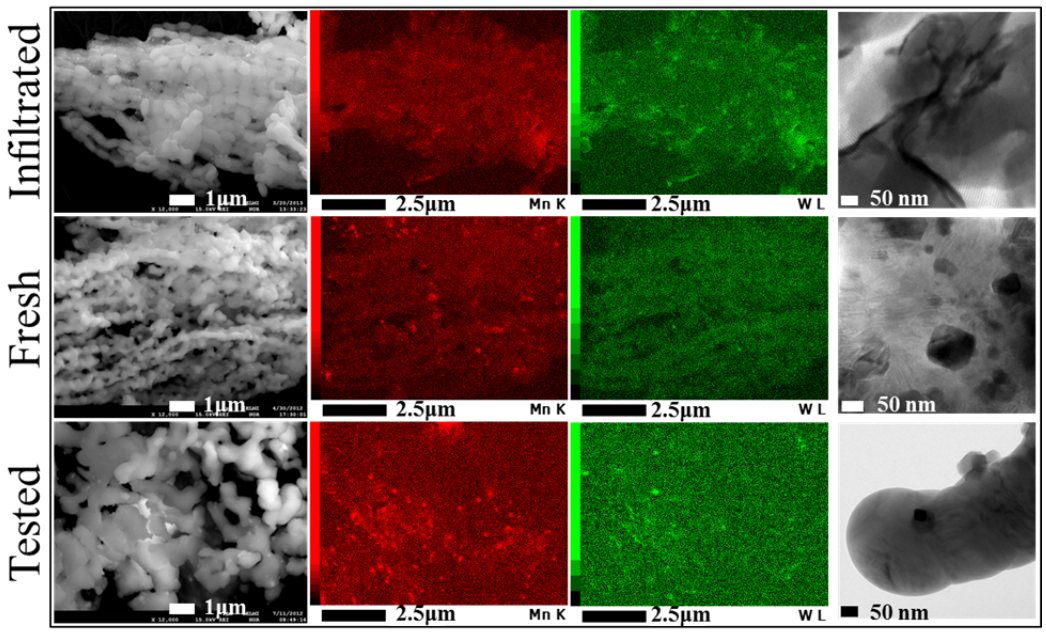

Figure 5. Electron micrograph investigation of Cat-H. SEM (left) (corresponding to EDX-mapping of manganese (red) and tungsten (green)) and TEM (right) images for the different treated catalyst (infiltrated, calcined, tested). Only SEM image of fresh Cat-H was reprinted from [41], with permission of The Royal Society of Chemistry.

Elemental mapping of the infiltrated catalyst precursor shows a homogeneous fine dispersion of manganese and tungsten. The fresh catalyst demonstrates a homogeneous distribution of tungsten while manganese can be found with local enrichments in patches all over the matrix. The catalytic testing of the material performed also particular enrichments of tungsten in addition to manganese.

Comparative investigations by TEM (Figure S28-S29) represents the existence of crystalline needle- and plate-like aggregates for the infiltrated sample. The formation of $MnWO_4$ (monoclinic-prismatic, P2/a) could be observed by high resolution TEM and Fast Fourier Transformation (FFT) (Figure S28-S29). However, in the calcined and tested catalyst, isolated particles of probably $MnMn_6SiO_{12}$ (ditetragonal-dipyramidal, $I4_1/acd$), Na_2WO_4 and/or $MnWO_4$ (monoclinic-prismatic, $P2/a$) with a typical morphology are detectable, also in good agreement with the detected phases of the *ex situ* XRD measurements. The crystalline needle-like aggregates could be only identified as thin bands, partially crystalline areas, that could be assigned as Na_2WO_4 phase (monoclinic-prismatic, $P2/a$) (Figure S28-S29). Finally, the high surface area (616.9 m^2/g) of the silica support SBA-15 and the presence of an ordered pore structure result in a highly homogeneous element distribution and fixation during infiltration process.

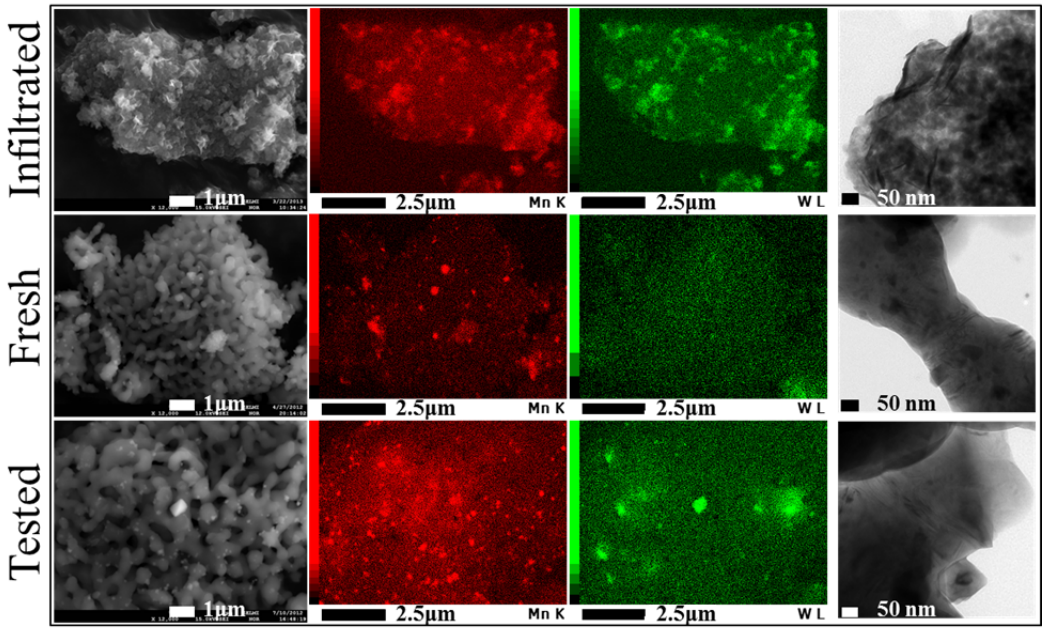

Figure 6. Electron micrographs of Cat-M. SEM (left) (corresponding to EDX-mapping of manganese (red) and tungsten (green)) and TEM (right) images for the different treated catalyst (infiltrated, calcined, tested).

SEM images of Cat-M are characterised by a flake-like morphology (infiltrated catalyst), while the fresh and tested catalyst features a continuous gross-porous morphology (Figure 6). Compared to Cat-H, the distribution of the relevant elements manganese and tungsten is more inhomogeneous in the infiltrated Cat-M precursor. Similar to Cat-H, the fresh catalyst represents a local enrichment of manganese (single particles) and a homogeneous distribution of tungsten, the tested catalyst features a local enrichment of both tungsten and manganese comprised with the formation of larger single crystalline particles.

In addition, TEM measurements (Figure S30) show crystalline fibrous and plate-like growth morphologies for the infiltrated catalyst precursor similar to those of Cat-H. A first formation of $MnWO_4$ could be expected. The fresh, as well as the tested catalyst features the crystallization of aggregates with pyramidal and/or prismatic morphology, probably $MnMn_6SiO_{12}$ (ditetragonal-dipyramidal, $I4_1/acd$), Na_2WO_4 and/or $MnWO_4$ (monoclinic-prismatic, $P2/a$). That identification can be supported by the XRD measurements. The needle-like aggregates become smaller, but demonstrate a homogeneous distribution in the silica matrix. Finally, the smaller surface area (105.4 m^2/g) and the unordered structure of Cat-M leads to an inhomogeneous distribution of manganese and tungsten during the infiltration process. Thus, the material shows a medium performance.

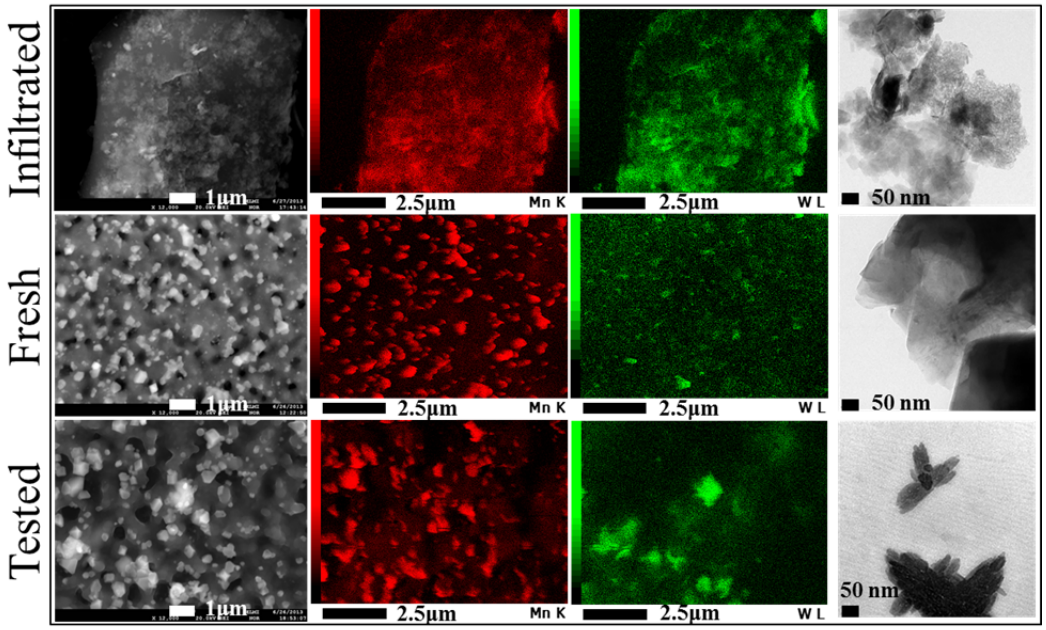

Figure 7. Electron micrographs of Cat-L. SEM (left) (corresponding to EDX-mappings of manganese (red) and tungsten (green)) and TEM (right) images for the different treated catalyst (infiltrated, calcined, tested).

Cat-L demonstrates a completely different morphology compared to Cat-H and Cat-M (Figure 7). The infiltrated catalyst precursor features small crystalline particles embedded in and/or growth on an amorphous/glassy matrix. The size of the particles increases after calcination under air at 750 °C dramatically (max. 500 nm) and grows still larger for the tested catalyst (max. 1 µm). Thus, the infiltrated precursor shows an inhomogeneous distribution of tungsten and manganese similar to Cat-M. For the fresh and tested catalyst, strong local enrichment of manganese and only a few local enrichment of tungsten is observed.

TEM images (Figure S31) illustrate the existence of large particles with needle- and plate-like morphology for the infiltrated sample. $MnWO_4$ phase could be identified as crystalline phase by high resolution TEM and selected area electron diffraction

576 (SAED) (Figure S32). Large crystals of Na_2WO_4 particles are observed in the fresh
577 catalyst. The tested Cat-L represents crystals with a typical pyramidal and/or prismatic
578 morphology as well as particles that consist of an agglomeration of plate-like aggregates
579 (Na_2WO_4 or $MnWO_4$, Figure S31). These observations are in good agreement with the
580 XRD results. Generally, Cat-L shows large crystalline particles leading to the lower
581 performance of that material, as will be shown in catalysis part.
582
583 **3.3.3. Catalysis**
584 The results recorded via a single reactor set-up using a packed-bed, U-shaped, tubular
585 reactor made of quartz glass are shown for the first 5 h at 725 °C, for the second 5h at
586 750 °C and for the last 5 h at 775 °C in Figure 8. Equal amounts of Cat-H, Cat-M and
587 Cat-L (100 mg) diluted with quartz sand were tested inside the quartz reactor.
588 The CH_4 conversion of the catalysts increases with increasing temperature and
589 the activity difference becomes higher at higher temperatures. However, it is clearly
590 seen that Cat-H always shows higher CH_4 conversion than Cat-M and Cat-L even at
591 different temperatures. The CH_4 conversion data of the catalysts exhibit the highest
592 values at 775 °C with approximately 25% for Cat-H, 18% for Cat-L and 3% for Cat-L.
593 Under reaction conditions at 725 °C, 750 °C and 775 °C the catalysts were very stable,
594 almost no deactivation was observed at the end of all experiments.
595 Cat-H is always more selective towards the formation of C_2 products
596 (C_2H_6+C_2H_4) than Cat-M. However, Cat-H even performed with higher CH_4 conversion
597 at higher C_2 selectivities in comparison to Cat-M. By using SBA-15, the Mn_xO_y-
598 Na_2WO_4/SiO_2 catalyst was improved in terms of both, activity and selectivity. At 775
599 °C the C_2 selectivity of Cat-L is higher than those of Cat-H and Cat-M, but showing

very poor CH_4 conversion. With respect to the C_2 yield, Cat-H is superior to Cat-M and Cat-L for all temperatures.

The CO selectivities of the Cat-H and Cat-M were very similar and decreases with increasing temperature, while no CO was observed for Cat-L catalyst. Differences between CO_2 selectivity results become lower with increasing temperature and CO_2 selectivity exhibits also similar decreasing trend with increasing temperature as seen for the CO selectivity. While Cat-H and Cat-M produced similar amounts of C_2H_6 at different temperatures, especially at 750 °C and 775 °C, Cat-H showed higher C_2H_4 selectivity than Cat-M at all these temperatures.

For the results presented in Figure 8, the same amount of each catalyst was tested. However, surface areas of the catalysts inside the reactors were different, when amount of catalyst was kept constant. Therefore, appropriate amounts of each catalyst were tested in order to get the same surface area inside the reactors. These results allowed to make more precise comparison between Cat-H, Cat-M and Cat-L (Figure S33).

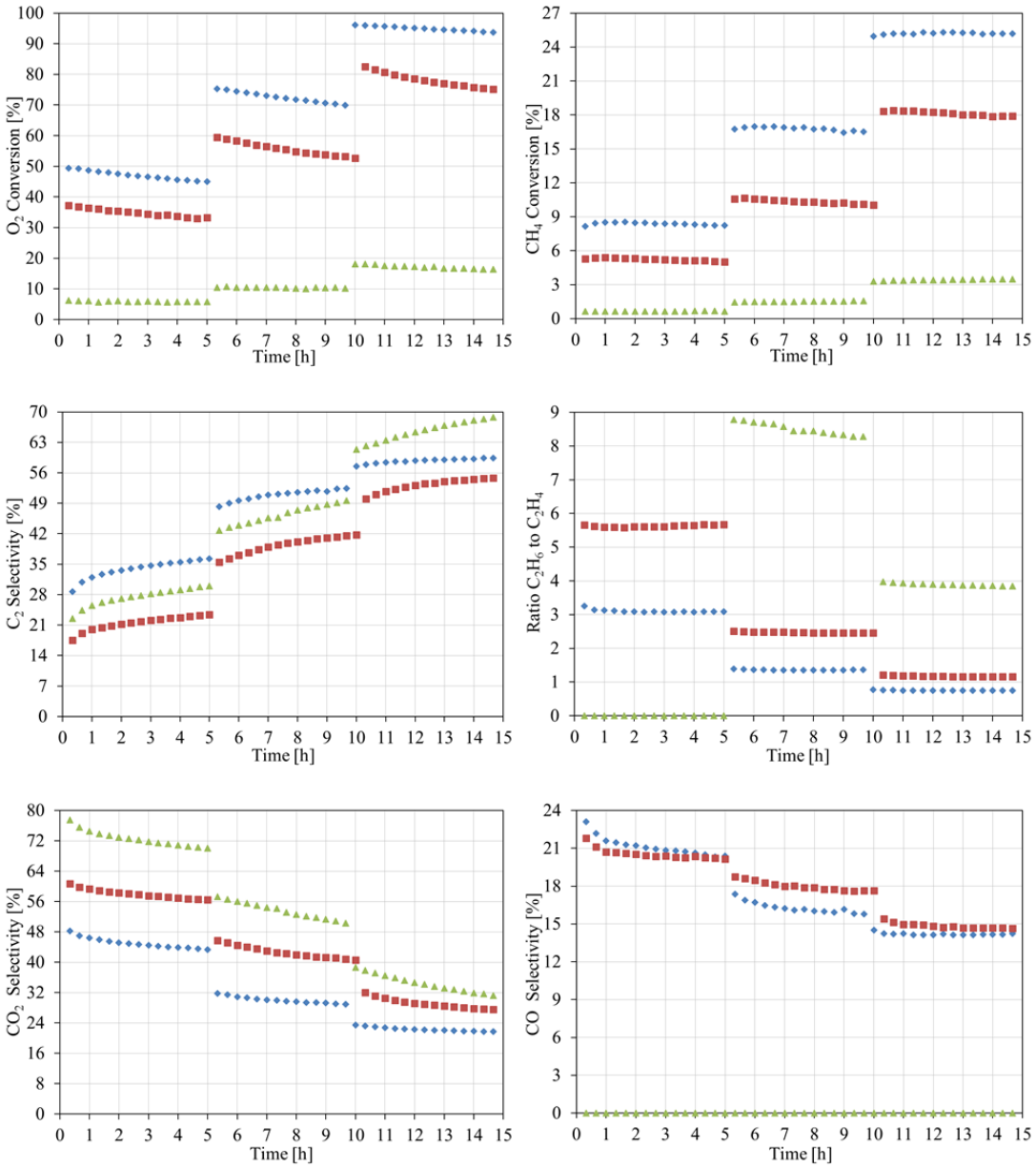

Figure 8. Catalytic activity test results of Cat-H (♦), Cat-M (■) and Cat-L (▲) catalysts (same amount of each catalyst is present inside the reactor). Reaction conditions: 725 °C, 750 °C, 775 °C, 100 mg catalyst diluted in 1.5 ml quartz sand, particle size of catalyst ≤ 200 µm, flow rate of 60 ml/min and feed gas composition of CH_4:O_2:N_2 = 4:1:4. Graphs show the O_2 and CH_4 conversion of reactant in the first row, the C_2 selectivity and the ratio of C_2H_6/C_2H_4 in the second row and the CO_2 and CO selectivities in the third row.

Figure 9-11 present C_2 selectivity vs. CH_4 conversion diagrams of Cat-H, Cat-M and Cat-L, respectively. In order to compare the performances of the catalysts more precisely, different flow rates (30, 40, 50, 60, 70, 80, 90, 100, 110, 120, 130, 140, 150 and 160 in ml/min) at different temperatures were applied for the experiments in the single reactor set-up to derive X-S diagrams. 100 mg catalyst diluted in 1.5 ml quartz sand and the feed gas composition of CH_4:O_2:N_2 = 4:1:4 was used for the experiments.

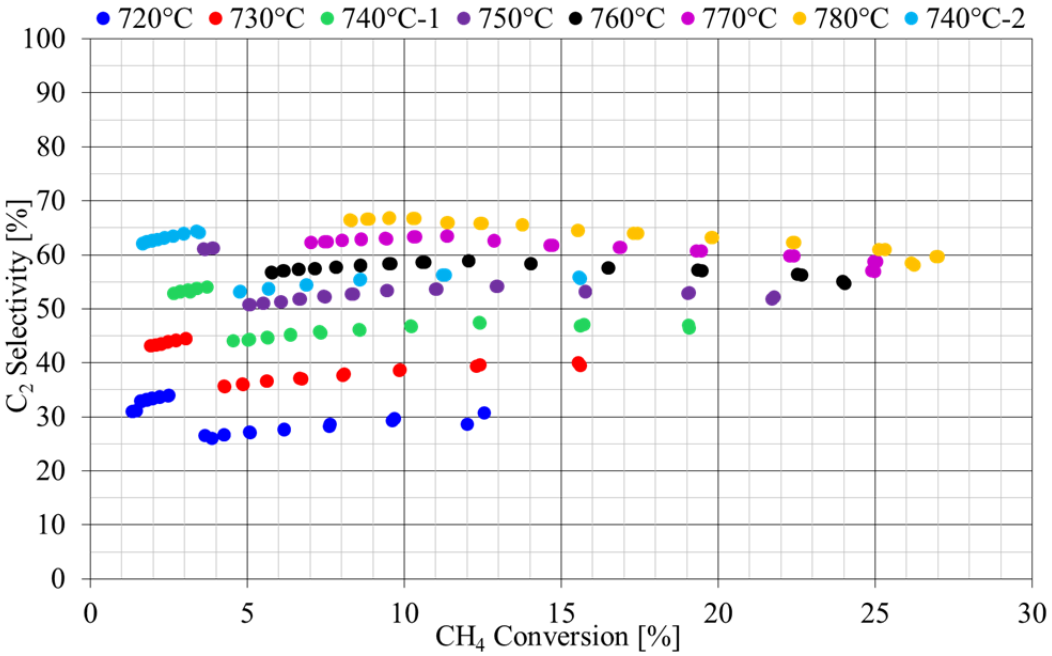

Figure 9. Methane conversion-C_2 selectivity diagram of Cat-H (100 mg catalyst diluted in 1.5 ml quartz sand, CH_4:O_2:N_2 = 4:1:4).

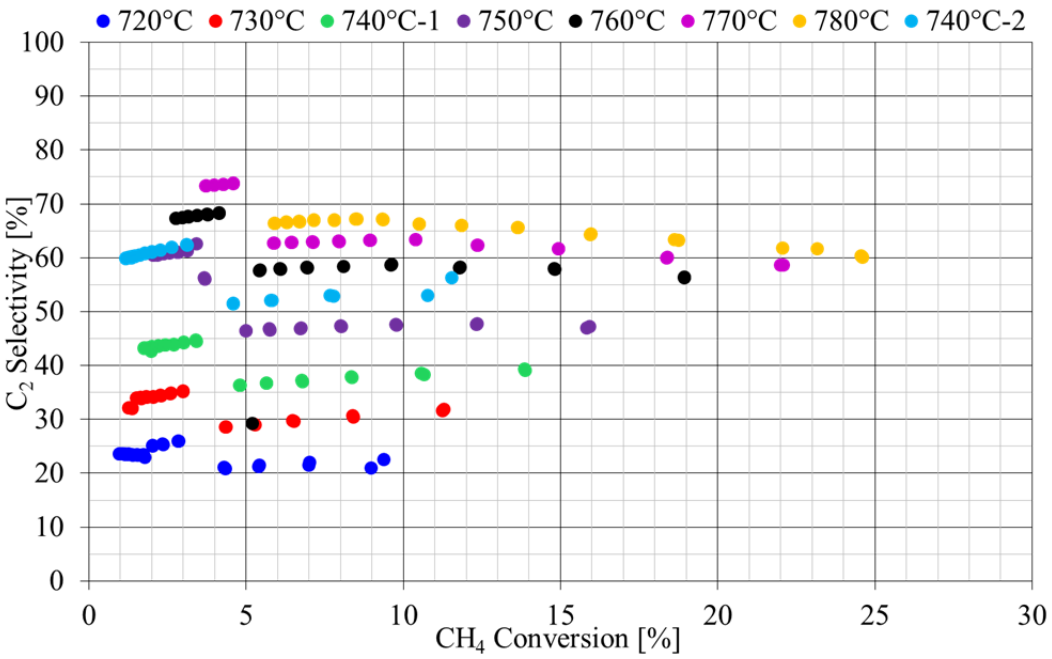

642

643 Figure 10. Methane conversion-C_2 selectivity diagram of Cat-M (100 mg catalyst

644 diluted in 1.5 ml quartz sand, CH_4:O_2:N_2 = 4:1:4).

645

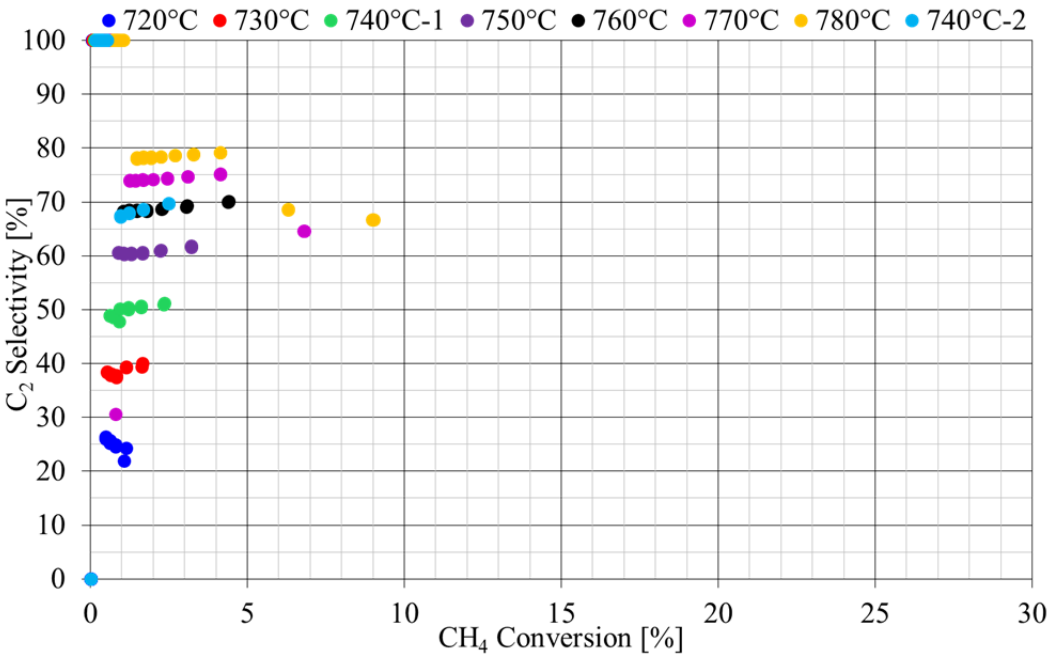

646

647 Figure 11. Methane conversion-C_2 selectivity diagram of Cat-L (100 mg catalyst diluted

648 in 1.5 ml quartz sand, CH_4:O_2:N_2 = 4:1:4).

649

650 At high flow rates, because of low contact time, the CH_4 conversion is low, in
651 particular at 720 °C, 730 °C, 740 °C and some at 750 °C for Cat-H (Figure 9).
652 Decreasing flow rate increases the CH_4 conversion at nearly constant C_2 selectivity. The
653 scattering of data points expands towards higher CH_4 conversions with increasing
654 temperature and decreasing flow rate. The highest CH_4 conversion (27%) was obtained
655 at 780 °C during reactant flow of 40 ml/min at 60% C_2 selectivity (Figure 9). While
656 there are definitely better results in terms of C_2 yield (18-25%) in literature by applying
657 the Mn_xO_y-Na_2WO_4/SiO_2 catalyst [20, 29, 31, 32, 38, 43], it has been also presented
658 similar or lower C_2 yield values (5-16%) in some publications [28, 33, 48, 49]. The
659 scattering in catalytic activity results can be clearly seen in Figure 12, a comparison of
660 Mn_xO_y-Na_2WO_4/SiO_2 catalysts presented in literature with the results of Cat-H, Cat-M
661 and Cat-L catalysts recorded for the experiments of the X-S graphs (Figure 9-11).
662 However the reason of this fact can be explained that catalytic activity results for the
663 OCM depends strongly on the different factors, e.g. temperature, flow rate, CH_4/O_2
664 ratio, inert gas and catalyst bed dilution, amount of used catalyst, active metal loadings,
665 etc. as stated in [50]. The presented results are the best results among the used SiO_2
666 supported catalysts under the given conditions in this study. Since the main aim of the
667 paper is to investigate the SiO_2 support effects and compare the produced catalysts, a
668 proper and detailed performance optimization of Cat-H is not in the scope of this work.
669 Therefore, the performance of Cat-H might be improved to be rivalled the present high
670 C_2 yield values in literature applying very different reaction conditions and parameters.

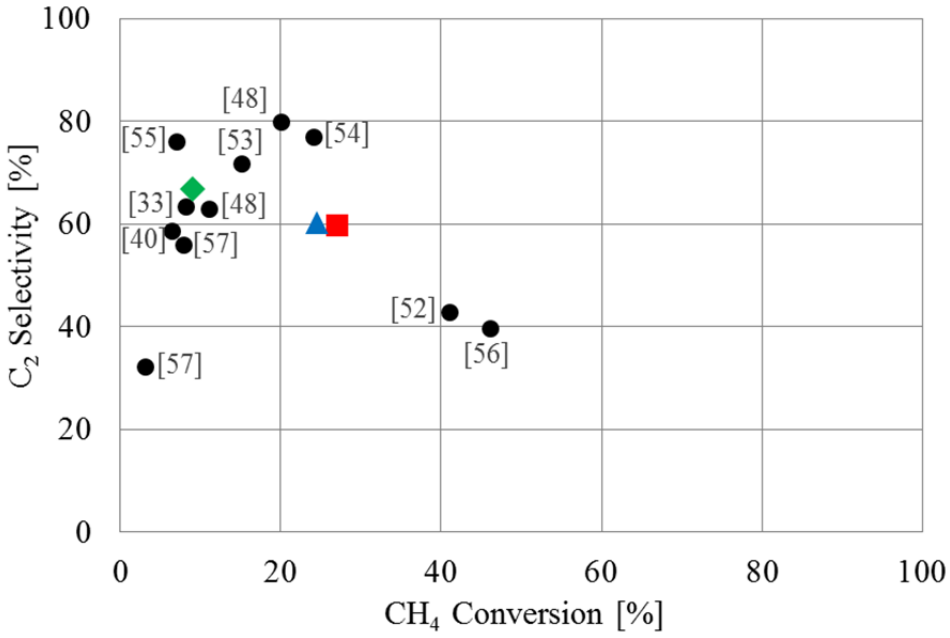

Figure 12. A catalytic activity comparison of some Mn_xO_y-Na_2WO_4/SiO_2 catalysts published in literature with our best results (♦: Cat-L, ▲: Cat-M and ■: Cat-H) recorded in the X-S graph experiments (temperatures of the catalytic tests differ between 700-780°C and results of higher temperatures than 780°C have been left out).

After the data points had been recorded at 780 °C, the temperature was decreased to 740 °C (740 °C-2) for the second time. In comparison to the results obtained at 740 °C-1, the results of 740 °C-2 were slightly different. While the CH_4 conversion was decreasing, the C_2 selectivity has increased. The reason could be structural changes of the catalyst at the high temperature under reaction conditions [51].

The X-S diagram of Cat-M (Figure 10) catalyst is also very similar to that of Cat-H. Cat-M catalyst showed the best performance at 780 °C with 24.6% CH_4 conversion and 60% C_2 selectivity under 30 ml/min flow rate of reactant (Figure 10). The prominent difference is that the distribution of the data points of Cat-M towards higher conversion values is lower than that of Cat-H. Another distinct point is that the

performance differences of Cat-M in terms of C_2 yield obtained 740 °C-1 and 740 °C-2 are higher than in the case of Cat-H. Figure 11 demonstrates that Cat-L is almost inactive for the OCM. Nearly all data points are below 5% CH_4 conversion. The highest CH_4 conversion was 9% at approximately 67% C_2 selectivity at 30 ml/min reactant flow at 780 °C.

For investigating the effect of catalyst bed dilution on the catalytic performance, we performed experiments for Cat-H, Cat-M and Cat-L catalysts diluted in different amount of quartz sand (1 and 2 ml).

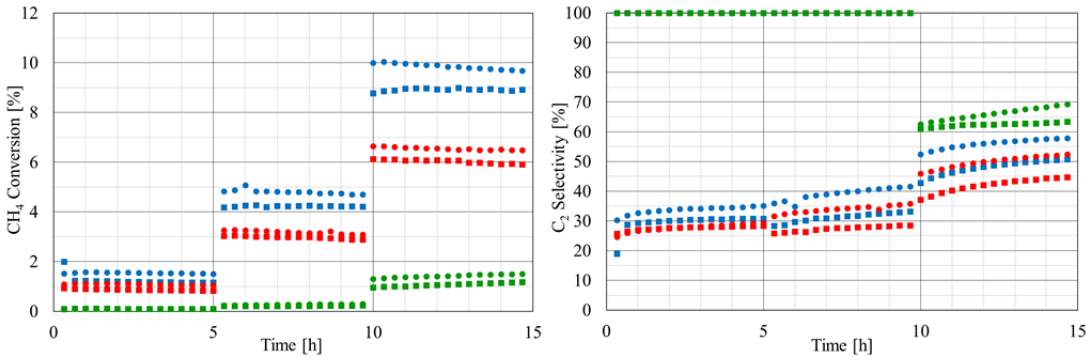

Figure 13. Catalytic performances of Cat-H (●: 1 ml, ■: 2 ml), Cat-M (●: 1 ml, ■: 2 ml) and Cat-L (●: 1 ml, ■: 2 ml) catalysts in different amounts of dilution (CH_4:O_2:N_2 = 4:1:4, 60 ml/min, 40 mg catalyst diluted in 1.5 ml quartz sand). The results were recorded for the first 5 h at 725°C, for the second 5h at 750°C and for the last 5 h at 775°C in single reactor set-up.

Figure 13 shows the CH_4 conversions and C_2 selectivities of the experiments. The difference between CH_4 conversions of the differently diluted catalysts increased slightly with increasing temperature. CH_4 conversions of catalysts diluted in 2 ml quartz sand were a little lower than the catalysts diluted in 1 ml quartz sand. However, these differences are within the range of deviation of the set-up. The C_2 selectivities of Cat-L

are not discussed because of very low CH_4 conversions at 725 °C and 750 °C. At these temperatures C_2 selectivities of Cat-H and Cat-M showed a similar tendency like in the CH_4 conversion. At 775 °C, all catalysts with 2 ml catalyst bed were a little less selective towards C_2 products than the catalysts with 1 ml catalyst bed dilution, indicating unselective gas phase side reactions in the extended void fraction of the catalyst bed.

4. Summary & Conclusion

Mn_xO_y-Na_2WO_4/SiO_2 catalysts were prepared and characterized by applying purchased and produced silica support materials.

In the S2 type silica supported catalyst a $MnWO_4$ phase was detected and it was assumed in the beginning that the reasons for the low performance of the S2 type supported catalyst were its low surface area and an additional $MnWO_4$ phase. Besides that, S11 type silica (SBA-15) supported catalyst showed an outstanding performance with high methane conversion and C_2 selectivity (also shown in [41]), while the rest of the catalysts performed very similar to each other.

Although same preparation method, active compound precursors and test conditions were applied for all silica supported catalysts, the catalytic performances of some catalysts (Cat-H, Cat-M and Cat-L) were interestingly very different. It is evident that the silica support material of the Mn_xO_y-Na_2WO_4 catalyst system plays an important role in the activity and the performance of the OCM.

In the XRD phase analysis of Cat-L (corresponding to S2 supported catalyst), no $MnWO_4$ phase was detected. Therefore it is evident that $MnWO_4$ is not the reason for the low performance of S2 supported catalyst in the silica variation part. Furthermore,

731 the $MnWO_4$ phase was also detected in Cat-H (SBA-15 supported catalyst) which
732 shows high performance in the OCM.

733 During the *in situ* XRD analysis of RCat-H (reproduced Cat-H), RCat-M
734 (reproduced Cat-M) and RCat-L (reproduced Cat-L), the main phase was α-cristobalite.
735 The observation of quartz phase formation revealed a structural change of the silica
736 support material. Three different phases of silica material were present during the
737 analyses of the catalysts. $MnWO_4$ was the only detected phase, which included the
738 starting metal oxide materials.

739 It was shown in the *in situ* XRD analysis of the calcination process of the
740 catalysts that the transformation of amorphous silica into crystalline α-cristobalite phase
741 started at different temperature levels for each catalyst ($T_{RCat\text{-}L}>T_{RCat\text{-}M}>T_{RCat\text{-}H}$). This
742 could cause different crystallization rates during calcination.

743 According to the SEM-EDX analysis, more homogeneous dispersion of the
744 active metal oxides for the Cat-H and inhomogeneous dispersion for the Cat-M and Cat-
745 L were observed.

746 The catalytic activity tests performed at different temperatures with different
747 flow rates are presented in X-S diagrams for Cat-H, Cat-M and Cat-L. Besides that, the
748 experiments, which were carried out by providing same surface areas of the catalysts,
749 revealed that in Cat-H the number of active sites responsible for the OCM was higher
750 than those of Cat-M and Cat-L. These presented results proved clearly that the
751 performance of Cat-H catalyst is superior to Cat-M and Cat-L catalysts for the OCM.

752 The obvious conclusion can also be drawn that the precursor of the silica support
753 material during catalyst preparation has a strong influence on the performance of the
754 Mn_xO_y-Na_2WO_4/SiO_2 system. Among all the used silica support materials in this work,

the SBA-15 was the best for the Mn_xO_y-Na_2WO_4 active metal oxides. The reason for the high performance of the Mn_xO_y-Na_2WO_4/SBA-15 catalyst can be explained by the more homogeneous dispersion of active compounds and higher number of active sites responsible for the OCM.

As it can be seen in the *in situ* XRD experiments during OCM and SEM images after the OCM, some structural changes occur in the Mn_xO_y-Na_2WO_4/SiO_2 system under reaction conditions. This indicates that under reaction conditions the catalysts become different materials than the fresh catalysts. Therefore, it would be very interesting to perform other *in situ* characterization methods cooperated with catalytic activity tests for unravelling the structure-activity relationship of this catalyst.

Abbreviations

BET	Brunauer Emmett Teller
C_2	Ethane + Ethylene
EDX	Energy-Dispersive X-Ray Spectroscopy
FID	Flame Ionization Detector
OCM	Oxidative Coupling of Methane
S	Selectivity
SEM	Scanning Electron Microscopy
TCD	Thermal Conductivity Detector
TEM	Transmission Electron Microscopy
UHV	Ultra High Vacuum
X	Conversion
XPS	X-Ray Photoelectron Spectroscopy

XRD X-Ray Diffraction

XRF X-Ray Fluorescence

Acknowledgement

This work is part of the Cluster of Excellence "Unifying Concepts in Catalysis" coordinated by the Technische Universität Berlin. Financial support by the Deutsche Forschungsgemeinschaft (DFG) within the framework of the German Initiative for Excellence is gratefully acknowledged. Mr. Yildiz is obliged to the Ministry of Education of the Republic of Turkey for fundings. We would like to thank Prof. Dr. Robert Schlögl from the Fritz Haber Institute of the Max Planck Society for allowing us to use the instrument for *in situ* XRD characterizations. We thank also Dr. Olaf Timpe and Rafael Zubrzycki for XRF measurements. We thank Harald Link for ICP measurements and Maria Unterweger for XRD measurements. We are also obliged to Mr. Schiele and the workshop for their support with the equipment and Mr. Reichert and his team for repairing and preparing used glass devices. Moreover, we would like to thank Evonik and BASF for supplying support material.

References

[1] BP, BP Statistical Review of World Energy June 2015, Online, Available at: https://www.bp.com/content/dam/bp/pdf/energy-economics/statistical-review-2015/bp-statistical-review-of-world-energy-2015-full-report.pdf, Last Accessed: December 28th, 2015.

[2] S. Arndt, R. Schomäcker, in: J. Reedijk (Ed.), Reference Module in Chemistry, Molecular Sciences and Chemical Engineering, Elsevier, Waltham, MA, 2014, pp. 1-15.

[3] A. Holmen, Catal. Today 142 (2009) 2-8.

[4] J.H. Lunsford, Angew. Chem. Int. Edit. 34 (1995) 970-980.

[5] J. H. Lunsford, Catal. Today 63 (2000) 165-174.

[6] P. Tang, Q. Zhu, Z. Wu, D. Ma, Energ. Environ. Sci. 7 (2014) 2580-2591.

[7] X. Guo, G. Fang, G. Li, H. Ma, H. Fan, L. Yu, C. Ma, X. Wu, D. Deng, M. Wei, D. Tan, R. Si, S. Zhang, J. Li, L. Sun, Z. Tang, X. Pan, X. Bao, Science 344 (2014) 616-619.

[8] R. Horn, R. Schlögl, Catal. Lett. 145 (2015) 23-39.

[9] A. M. Maitra, Appl. Catal. A-Gen. 104 (1993) 11-59.

[10] U. Zavyalova, M. Holena, R. Schlögl, M. Baerns, ChemCatChem 3 (2011) 1935-1947.

[11] E.V. Kondratenko, M. Schlüter, M. Baerns, D. Linke, M. Holena, Catal. Sci. Technol. 5 (2015) 1668.

[12] G.E. Keller, M.M. Bhasin, J. Catal. 73 (1982) 9-19.

[13] W. Hinsen, M. Baerns, Chem. Ztg. 107 (1983) 223-226.

[14] E.V. Kondratenko, M. Baerns, in: G. Ertl, H. Knözinger, F. Schüth, J. Weitkamp (Eds.), Handbook of Heterogeneous Catalysis, Wiley-VCH Verlag GmbH & Co. KGaA, Weinheim, 2008, pp. 3010-3023.

[15] S. Arndt, G. Laugel, S. Levchenko, R. Horn, M. Baerns, M. Scheffler, R. Schlögl, R. Schomäcker, Catal. Rev. 53 (2011) 424-514.

[16] S. Arndt, U. Simon, S. Heitz, A. Berthold, B. Beck, O. Görke, J.D. Eppinger, T. Otremba, Y. Aksu, E. Irran, G. Laugel, M. Driess, H. Schubert, R. Schomäcker, Top. Catal. 54 (2011) 1266-1285.

[17] X. Fang, S. Li, J. Lin, Y. Chu, J. Mol. Catal. (China) 6 (1992) 427-433.

827 [18] X. Fang, S. Li, J. Lin, J. Gu, D. Yan, J. Mol. Catal. (China) 6 (1992) 255-262.
828 [19] A. Vamvakeros, S.D.M. Jacques, V. Middelkoop, M. Di Michiel, C.K. Egan,
829 I.Z. Ismagilov, G.B.M. Vaughan, F. Gallucci, M. van Sint Annaland, P.R.
830 Shearing, R.J. Cernik, A.M. Beale, Chem. Commun. 51 (2015) 12752-12755.
831 [20] S. Sadjadi, U. Simon, H.R. Godini, O. Görke, R. Schomäcker, G. Wozny, Chem.
832 Eng. J. 281 (2015) 678-687.
833 [21] H. R. Godini, S. Jašo, Shengnan Xiao, H. Arellano-Garcia, M. Omidkhah, G.
834 Wozny, Ind. Eng. Chem. Res. 51 (2012) 7747-7761.
835 [22] H.R. Godini, H. Trivedi, A. Gili de Villasante, O. Görke, S. Jašo, U. Simon, A.
836 Berthold, W. Witt, G. Wozny, Chem. Eng. Res. Des. 91 (2013) 2671-2681.
837 [23] H. R. Godini, A. Gili, O. Görke, U. Simon, K. Hou, G. Wozny, Energ. Fuel. 28
838 (2014) 877-890.
839 [24] H. R. Godini, S. Xiao, M. Kim, N. Holst, S. Jašo, O. Gorke, J. Steinbach, G.
840 Wozny, J. Ind. Eng. Chem. 20 (2014) 1993-2002.
841 [25] S. Jašo, H.R. Godini, H. Arellano-Garcia, M.Omidkhah, G.Wozny, Chem. Eng.
842 Sci. 65 (2010) 6341-6352.
843 [26] S. Jašo, H. Arellano-Garcia, G. Wozny, Chem. Eng. J. 171 (2011) 255-271.
844 [27] S. Jašo, S. Sadjadi, H. R. Godini, U. Simon, S. Arndt, O. Görke, A. Berthold, H.
845 Arellano-Garcia, H. Schubert, R. Schomäcker, G. Wozny, J. Nat. Gas Chem. 21
846 (2012) 534-543.
847 [28] S. Arndt, T. Otremba, U. Simon, M. Yildiz, H. Schubert, R. Schomäcker, Appl.
848 Catal. A-Gen. 425-426 (2012) 53-61.
849 [29] R. Ghose, H.T. Hwang, A. Varma, Appl. Catal. A-Gen. 452 (2013) 147-154.
850 [30] R. Ghose, H.T. Hwang, A. Varma, Appl. Catal. A-Gen. 472 (2014) 39-46.

851 [31] H.R. Godini, A. Gili, O. Görke, S. Arndt, U. Simon, A. Thomas, R. Schomäcker,
852 G. Wozny, Catal. Today 236 (2014) 12-22.
853 [32] R. Koirala, R. Büchel, S.E. Pratsinis, A. Baiker, Appl. Catal. A-Gen. 484 (2014)
854 97-107.
855 [33] N. Hiyoshi, T. Ikeda, Fuel Process. Technol. 133 (2015) 29-34.
856 [34] H. Liu, D. Yang, R. Gao, L. Chen, S. Zhang and X. Wang, Catal. Commun. 9
857 (2008) 1302-1306.
858 [35] Z. Yu, X. Yang, J. Lunsford, M. Rosynek, J. Catal. 154 (1995) 163-173.
859 [36] D. Wang, M. Rosynek, J. Lunsford, J. Catal. 155 (2) (1995) 390-402.
860 [37] S. Pak, P. Qiu, J. Lunsford, J. Catal. 179 (1) (1998) 222-230.
861 [38] T.W. Elkins, H.E. Hagelin-Weaver, Appl. Catal. A-Gen. 497 (2015) 96-106.
862 [39] T. Serres, C. Aquino, C. Mirodatos, Y. Schuurman, Appl. Catal. A-Gen. 504
863 (2015) 509-518.
864 [40] M. Yildiz, U. Simon, T. Otremba, Y. Aksu, K. Kailasam, A. Thomas, R.
865 Scomäcker, S. Arndt, Catal. Today 228 (2014) 5-14.
866 [41] M. Yildiz, Y. Aksu, U. Simon, K. Kailasam, O. Görke, F. Rosowski, R.
867 Schomäcker, A. Thomas, S. Arndt, Chem. Commun. 50 (2014) 14440-14442.
868 [42] M. Yildiz, S. Arndt, U. Simon, Y. Aksu, T. Otremba, A. Berthold, O. Görke, A.
869 Thomas, H. Schubert, R. Schomäcker, in: S. Ernst, U. Balfanz, S. Buchholz, J.
870 Lichtscheidl, M. Marchionna, F. Nees and E. Santacesaria (Eds.), Reducing the
871 Carbon Footprint of Fuels and Petrochemicals, DGMK Conference Book-2012-
872 3, Deutsche Wissenschaftliche Gesellschaft für Erdöl, Erdgas und Kohle e.V.,
873 Berlin, 2012, pp. 125-132.
874 [43] S. Sadjadi, S. Jašo, H. R. Godini, S. Arndt, M. Wollgarten, R. Blume, O. Görke,

875 R. Schomäcker, G. Wozny, U. Simon, Catal. Sci. Technol. 5 (2015) 942-952.
876 [44] A. Palermo, J. P. Holgado Vazquez, A. F. Lee, M. S. Tikhov, R. M. Lambert, J.
877 Catal. 177 (1998) 259-266.
878 [45] A. Palermo, J. P. H. Vazquez, R. M. Lambert, Catal. Lett. 68 (2000) 191-196.
879 [46] J.G. Wu, S.B. Li, J. Phys. Chem.-US 99 (1995) 4566-4568.
880 [47] A. F. Wells, Structural Inorganic Chemistry, Chapter 23, Oxford Univ. Press,
881 Oxford 1004, 1987.
882 [48] A. Malekzadeh, A. Khodadadi, M. Abedini, M. Amini, A. Bahramian, A.K.
883 Dalai, Catal. Commun. 2 (2001) 241-247.
884 [49] I.Z. Ismagilov, E.V. Matus, S.D. Vasil'ev, V.V. Kuznetsov, M.A. Kerzhentsev,
885 Z. R. Ismagilov, Kinet. Catal. 56 (4) (2015) 456-465.
886 [50] Z. Kalenik and E. E. Wolf in Methane Conversion by Oxidative Processes,
887 Chapter 1: The Role of Gas-Phase Reactions during Methane Oxidative
888 Coupling, Van Nostrand Reinhold (1992) 30-77.
889 [51] S. Arndt, B. Uysal, A. Berthold, T. Otremba, Y. Aksu, M. Driess, R.
890 Schomäcker, J. Nat. Gas Chem. 21 (2012) 581-594.
891 [52] J. Wang, L. Chou, B. Zhang, H. Song, J. Zhao, J. Yang, S. Li, J. Mol. Catal. A:
892 Chem. 245 (2006) 272-277.
893 [53] L. Chou, Y. Cai, B. Zhang, J. Niu, S. Ji, S. Li, React. Kinet. Catal. Lett. 76(2)
894 (2002) 311-315.
895 [54] A. Malekzadeh, M. Abedini, A.A. Khodadadi, M. Amini, H.K. Mishra and A.K.
896 Dalai, Catal. Lett. 84 (1-2) (2002) 45-51.
897 [55] U. Simon, O. Gorke, A. Berthold, S. Arndt, R. Schomacker, H. Schubert, Chem.
898 Eng. J. 168 (2011) 1352-1359.

899 [56] S. Mahmoodi, M.R. Ehsani, S.M. Ghoreishi, J. Ind. Eng. Chem. 16 (2010) 923-
900 928.
901 [57] A.A. Greish, L.M. Glukhov, E.D. Finashina, L.M. Kustov, J. Sung, K. Choo, T.
902 Kim, Mendeleev Commun. 19 (2009) 337-339.